

Activatable Semiconducting Theranostics: Simultaneous Generation and Ratiometric Photoacoustic Imaging of Reactive Oxygen Species In Vivo

Zhen Yang, Yunlu Dai, Chao Yin, Quli Fan,* Wansu Zhang, Justin Song, Guocan Yu, Wei Tang, Wenpei Fan, Bryant C. Yung, Jie Li, Xiang Li, Xiangchun Li, Yufu Tang, Wei Huang, Jibin Song,* and Xiaoyuan Chen*

Enhancing the generation of reactive oxygen species (ROS) is an effective anticancer strategy. However, it is a great challenge to control the production and to image ROS in vivo, both of which are vital for improving the efficacy and accuracy of cancer therapy. Herein, an activatable semiconducting theranostic nanoparticle (NP) platform is developed that can simultaneously enhance ROS generation while self-monitoring its levels through ratiometric photoacoustic (PA) imaging. The NP platform can further guide in vivo therapeutic effect in tumors. The theranostic NP platform is composed of: (i) cisplatin prodrug and ferric ion catalyst for ROS generation, a part of combination cancer therapy; and (ii) a ratiometric PA imaging nanoprobe consisting of inert semiconducting perylene-diimide (PDI) and ROS activatable near-infrared dye (IR790s), used in ratiometric PA imaging of ROS during cancer treatment. Ratiometric PA signals are measured at two near-infrared excitation wavelengths: 680 and 790 nm for PDI and IR790s, respectively. The measurements show highly accurate visualization of $\cdot\text{OH}$ generation in vivo. This novel ROS responsive organic theranostic NP allows not only synergistic cancer chemotherapy but also real-time monitoring of the therapeutic effect through ratiometric PA imaging.

Increasing oxidative stress induced by reactive oxygen species (ROS) in cancer cells has been considered an effective anticancer strategy.^[1–3] Such a process can cause oxidative damage to cellular components including DNA strand breakage, leading to cell apoptosis.^[4] Endogenous bioenergetic materials have been developed to produce ROS in cancer cells.^[5,6] In the tumor region, excessive cellular growth produces a number of

hydrogen peroxide (H_2O_2) metabolites, at concentrations as high as $1 \times 10^{-3} \text{ M}$.^[7] Metallic ions, such as Fe^{3+} ^[8] and Mn^{2+} ,^[9] enable the disproportionation of H_2O_2 to its downstream toxic ROS hydroxyl radical ($\cdot\text{OH}$). Thus, several therapeutic strategies have been developed based on such catalytic reactions to generate ROS in tumors. The strategies were assisted by the released metallic catalyst from the carriers, such as iron oxide (Fe_3O_4) nanoparticle (NP)^[10] and amorphous iron NPs.^[11] On the other hand, cisplatin is a food and drug administration (FDA)-approved anticancer drug, possessing nuclear DNA crosslinking ability, thus restraining cell division.^[12–15] Cisplatin also has the ability to activate nicotinamide adenine dinucleotide phosphate oxidase (NOX) and efficiently convert O_2 to $\text{O}_2^{\cdot-}$, which can be dismutated by superoxide dismutase enzyme to form H_2O_2 (main source of H_2O_2 production), causing an upsurge in cellular H_2O_2 .^[16,17] Thus, developing

multifunctional chemotherapeutic agents, containing both cisplatin and metallic ions, is desirable for enhanced therapeutic efficacy mediated by ROS generation.^[18]

Photoacoustic (PA) imaging, which provides high spatial resolution with deep tissue penetration, has been employed in noninvasive real-time imaging of inflammation, thrombosis, tumor, and other diseases.^[19–27] However, the detection

Dr. Z. Yang, Dr. C. Yin, Prof. Q. Fan, Dr. W. Zhang, Dr. J. Li, Dr. X. Li, Dr. X. Li, Dr. Y. Tang, Prof. W. Huang
Key Laboratory for Organic Electronics and Information Displays
& Institute of Advanced Materials (IAM)
Jiangsu National Synergetic Innovation Center for Advanced
Materials (SICAM)
Nanjing University of Posts & Telecommunications
Nanjing 210023, China
E-mail: iamqlfan@njupt.edu.cn

 The ORCID identification number(s) for the author(s) of this article can be found under <https://doi.org/10.1002/adma.201707509>.

DOI: 10.1002/adma.201707509

Dr. Z. Yang, Dr. Y. Dai, J. Song, Dr. G. Yu, Dr. W. Tang, Dr. W. Fan, Dr. B. C. Yung, Prof. X. Chen
Laboratory of Molecular Imaging and Nanomedicine (LOMIN)
National Institute of Biomedical Imaging and Bioengineering (NIBIB)
National Institutes of Health (NIH)
Bethesda, MD 20892, USA
E-mail: shawn.chen@nih.gov
Prof. J. Song
MOE Key Laboratory for Analytical Science of Food Safety and Biology
College of Chemistry
Fuzhou University
Fuzhou 350108, China
E-mail: jibin.song@nih.gov

of PA signal is intensity-dependent and thus is susceptible to some common analyte-insensitive artifacts that are hard to correct including photobleaching, local light deposition, and variations in PA probe concentrations and dimension of target analytes.^[28] Recently, a series of activatable PA probes have been reported to detect specific biomarkers and small molecules by molecular structural changes that lead to spontaneous signal responsive variations.^[29–31] Moreover, ratiometric PA measurements, which have increased analytical sensitivity, specificity, and accuracy, have been developed to replace absolute PA signal intensity measurements. Examples of these developments include disease-specific imaging of copper(II),^[32] pH,^[33,34] and methylmercury,^[35] all of which were developed based on ratiometric PA probes.^[36] Understanding ROS, the highly cytotoxic species that can be utilized to kill cancer cells, is imperative to the detection and treatment of many life-threatening diseases.^[37,38] However, it is still difficult to detect ROS or trace its generation in vivo. An infrared (IR) dye, IR790s, has been used in ROS detection for in vivo real-time monitoring of hepatotoxicity based on its reactivity

with ROS. The absorption intensity changes of IR790s have been demonstrated to reflect the ROS generation caused by drugs in the liver.^[39–41] Thus, IR790s combined with an inert interference-free PA signal can be functionalized as a ratiometric PA probe to monitor the generation of ROS in situ.

In this study, we report a novel semiconducting perylene diimide (PDI)-based theranostic NP that can simultaneously enhance ROS generation and self-monitor its levels by ratiometric PA imaging, thus facilitating real-time observation of anticancer chemotherapy effect in vivo. The theranostic NP (PDI-IR790s-Fe/Pt) with rod-like nanostructure was constructed by self-assembly of PDI-based cisplatin prodrug (PDI prodrug), IR790s, and chelated ferric ions. The PDI chemical structure was largely modified to synthesize a novel asymmetric PDI prodrug (Figure 1a) containing multifunctional group (Figures S1–12, Supporting Information). The polyphenols linked to one of the amide groups of PDI can coordinate with ferric ions, thus directing the self-assembly of PDI prodrug^[42] and initiating the Fenton reaction with H₂O₂ to produce toxic [•]OH in acid environments. A polyethylene glycol (PEG)

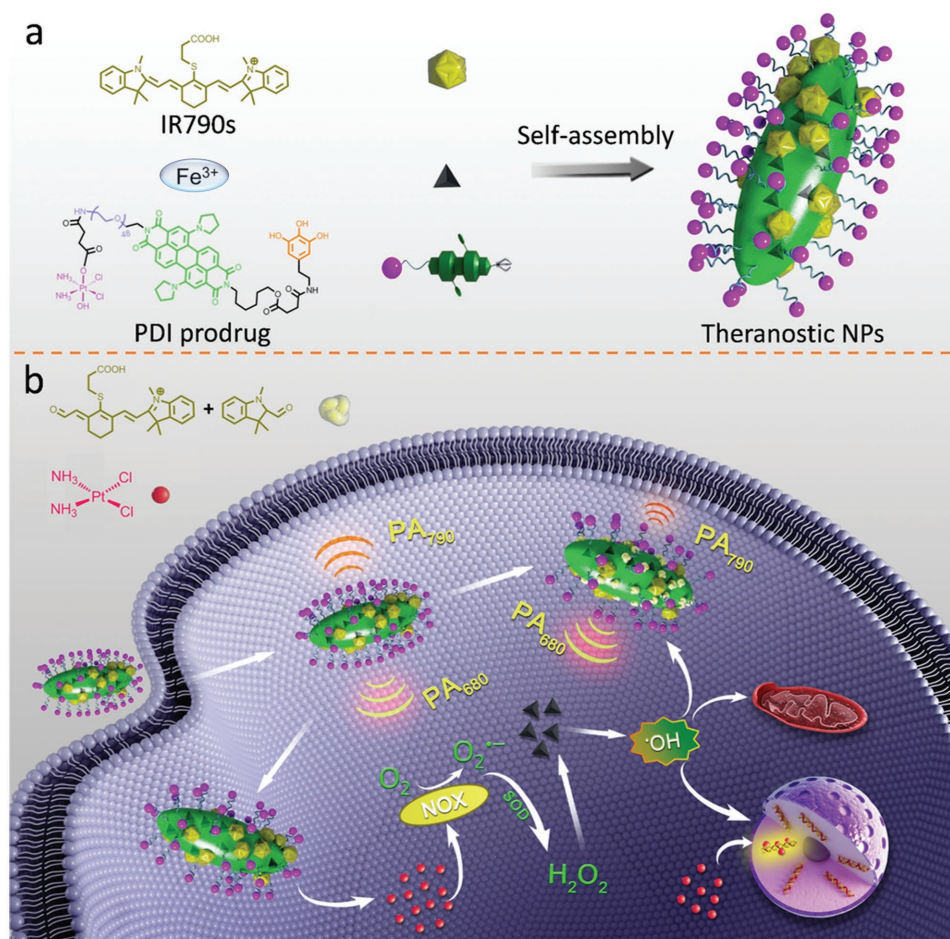


Figure 1. Preparation of PDI-based nanotheranostics and ratiometric photoacoustic (PA) imaging of the generated ROS in vivo. a) Schematic illustration of the preparation of theranostics by self-assembly of PDI prodrug and IR790s triggered by Fe³⁺, b) the released cisplatin from the theranostic NPs activates NOX, which catalyzes formation of H₂O₂ and superoxide from O₂. Then the Fe³⁺ turns H₂O₂ into highly toxic [•]OH by catalyzing the Fenton reaction. The generated [•]OH activates IR790s, leading to a PA signal change, while the PA signal from semiconducting PDI remains stable. Thus, the PA signal ratio of PDI and IR790s can be used for ratiometric PA imaging of the generated ROS.

chain was linked to the other amide group of PDI to promote water solubility and biocompatibility of the nanoplatform. A cisplatin prodrug (Figure S13, Supporting Information) was further conjugated to the free end of a PEG chain (Figure 1a). In the tumor microenvironment, cisplatin is released in the presence of reductive species such as glutathione and mediates the activation of NOX, triggering the conversion of oxygen (O_2) to superoxide radical ($O_2^{\cdot-}$), finally, leading to the downstream formation of H_2O_2 (Figure 1b). The H_2O_2 can further be catalyzed to toxic hydroxyl radicals ($\cdot OH$) by the loaded Fe^{3+} through the Fenton reaction. Moreover, PDI endows the NP platform with strong near infrared (NIR) absorption at 680 nm without bleaching by any photophysical or chemical interferences; and two pyrrolidines at the bay position make it a robust PA probe.^[43–46] An ROS-sensitive molecule, IR790s, has a strong and distinct absorption at 790 nm (despite some insignificant absorption at 680 nm). In the presence of ROS, IR790s can be cleaved into two oxides, diminishing its ability to absorb NIR light at 790 nm (Figure 1a). Therefore, these characteristics allow the theranostic nanoplatform to track ROS generation and cancer therapy effect by ratiometric PA imaging under excitation wavelengths of 680 and 790 nm.

To prepare the theranostic NPs, the self-assembly ability of PDI prodrug in water was first investigated. By taking advantage of the amphiphilic (hydrophilic–hydrophobic–hydrophilic) nanostructure of PDI prodrug, IR790s was encapsulated in PDI prodrug NPs by self-assembly in a solution containing dimethylformamide (DMF) and water (1:1, v/v). Due to the small proportion (volume) of hydrophobic PDI segments in relation to hydrophilic PEG and polyphenols, small-sized PDI prodrug NPs loaded with IR790s (average size: 17 ± 5.4 nm) were obtained without adding ferric ions (Figures S14–S15, Supporting Information). It is interesting to observe that large rod-like NPs were formed when ferric ions were added to the solution. It is possible that the π – π interaction of PDIs as well as the coordination between polyphenols of PDI prodrug and ferric ions were greatly increased. Thus, these two kinds of forces lead to π – π stacking of the perylene cores along 1D long axis without curvature, and the structure is stabilized by coordination between polyphenols and ferric ions and the surrounding PEGs as shown in Figure 1.^[47] Thus, the theranostic NPs, PDI–IR790s–Fe/Pt NPs, were obtained by the self-assembly of PDI prodrug and IR790s at a molar ratio of 30:1 in DMF, in the presence of ferric ions and water (which was added into the system). DMF was removed by dialysis against phosphate buffered saline (PBS) (pH 7.4) and the as-prepared NPs were stored in PBS. The mass ratio of Pt and Fe in the PDI–IR790s–Fe/Pt NPs was about 4.46:1 as measured by inductively coupled plasma mass spectrometry.

The transmission electron microscopy (TEM) images (Figure 2a) showed that rod-like theranostic NPs with an average diameter of 120 ± 33.5 nm were formed. After incubation in serum for 30 d, the diameters of theranostic NPs, according to the dynamic light scattering results, were nearly unchanged (Figure S16, Supporting Information). This indicates that the theranostic NPs are highly stable, which is likely due to strong π – π stacking interactions between PDI molecules and the coordination between ferric ions and polyphenols. Nevertheless, the coordination is not stable in an acidic environment, and can lead to

pH-responsive activity of theranostic NPs. Thus, the variations in size and morphology of NPs in different acidic environments were further investigated. In a buffer solution, pH 6.8, the theranostic NPs were larger and contained some nanopores on the surface (Figure 2a). Moreover, the NPs dissociated into smaller NPs or clusters in pH 5.0 buffer solution (Figure S17, Supporting Information), possibly due to a disruption in coordination. In following, exploiting the acidic environment of the tumor, PDI–IR790s–Fe/Pt NPs can be disassembled into smaller NPs, thus favoring their pH-responsive drug release and rapid clearance from the body.

To study the ROS-responsive ability of IR790s, PDI NPs loaded with IR790s (PDI–IR790s NPs) were prepared by the self-assembly of PDI structure 9 (Figure S1, Supporting Information) and IR790s. The UV–vis spectra displayed in Figure 2b showed that PDI–IR790s NPs (in aqueous solution) exhibited two strong absorption peaks at 680 and 790 nm corresponding to PDI and IR790s, respectively. To study their responsiveness to ROS following Fenton reaction, PDI–IR790s NPs were further incubated with H_2O_2 and Fe^{3+} . A H_2O_2 activity kit was utilized to monitor the concentration of H_2O_2 in aqueous solution, where absorption at 560 nm is observed when H_2O_2 is present. The decrease in absorption at 560 nm indicates that the consumption of H_2O_2 is activated by ferric ions, resulting in the production of $\cdot OH$. To quantitatively investigate ROS-responsive ability of NPs in producing $\cdot OH$, different amounts of $\cdot OH$ prepared by the reaction of H_2O_2 and $FeCl_3$ were incubated with PDI–IR790s NPs (3×10^{-6} M IR790s in 0.1 M PBS (pH 6.8)) and the UV–vis spectra and PA signals at 680 and 790 nm were then measured. The absorption intensity of PDI–IR790s NPs at 790 nm gradually decreased due to its ROS-responsive property, producing $\cdot OH$. In contrast, the absorption signal at 680 nm remained nearly unchanged (Figure 2c). The calculated absorption intensity ratio of 680 to 790 nm (Ab_{680}/Ab_{790}) was high in the presence of $\cdot OH$, while the ratio was low in H_2O_2 -treated NPs without the addition of ferric ions due to an absence of $\cdot OH$ generation (Figure 2d).

Because of the high sensitivity of PDI–IR790s to the generated $\cdot OH$ in the reaction of H_2O_2 and Fe^{3+} , we were encouraged to further investigate the ROS generation and the responsive properties of the theranostic PDI–IR790s–Fe/Pt NPs using UV–vis spectra and PA imaging. The PDI–IR790s–Fe/Pt NPs ($250 \mu g mL^{-1}$) were incubated with 0.1 M phosphate buffer (pH 6.8) and then treated with different concentrations of H_2O_2 (from 0 to 18×10^{-6} M). From the UV–vis spectra (Figure S18, Supporting Information), the absorption at 790 nm decreased with adding H_2O_2 . The correlation between Ab_{680}/Ab_{790} ratio and H_2O_2 concentration ranging from 0 to 18×10^{-6} M was linear. At a H_2O_2 concentration of 18×10^{-6} M, the Ab_{680}/Ab_{790} ratio was 4.25 ± 0.25 . The PA images and their corresponding signals at 680 and 790 nm were further measured. The PA spectrum of the PDI–IR790s–Fe/Pt NPs showed two strong PA intensity peaks at 680 and 790 nm (Figure 2e), which is consistent with their UV–vis spectra. After H_2O_2 was added into the system, the PA signal at 790 nm gradually decreased, while that at 680 nm remained almost constant. The PA images of the NPs at 680 and 790 nm were recorded in pseudo green and red colors, respectively. The color at 790 nm changed from white to dark red, while that at 680 nm was nearly unchanged (Figure 2f). The ratiometric PA signal at 680 to 790 nm

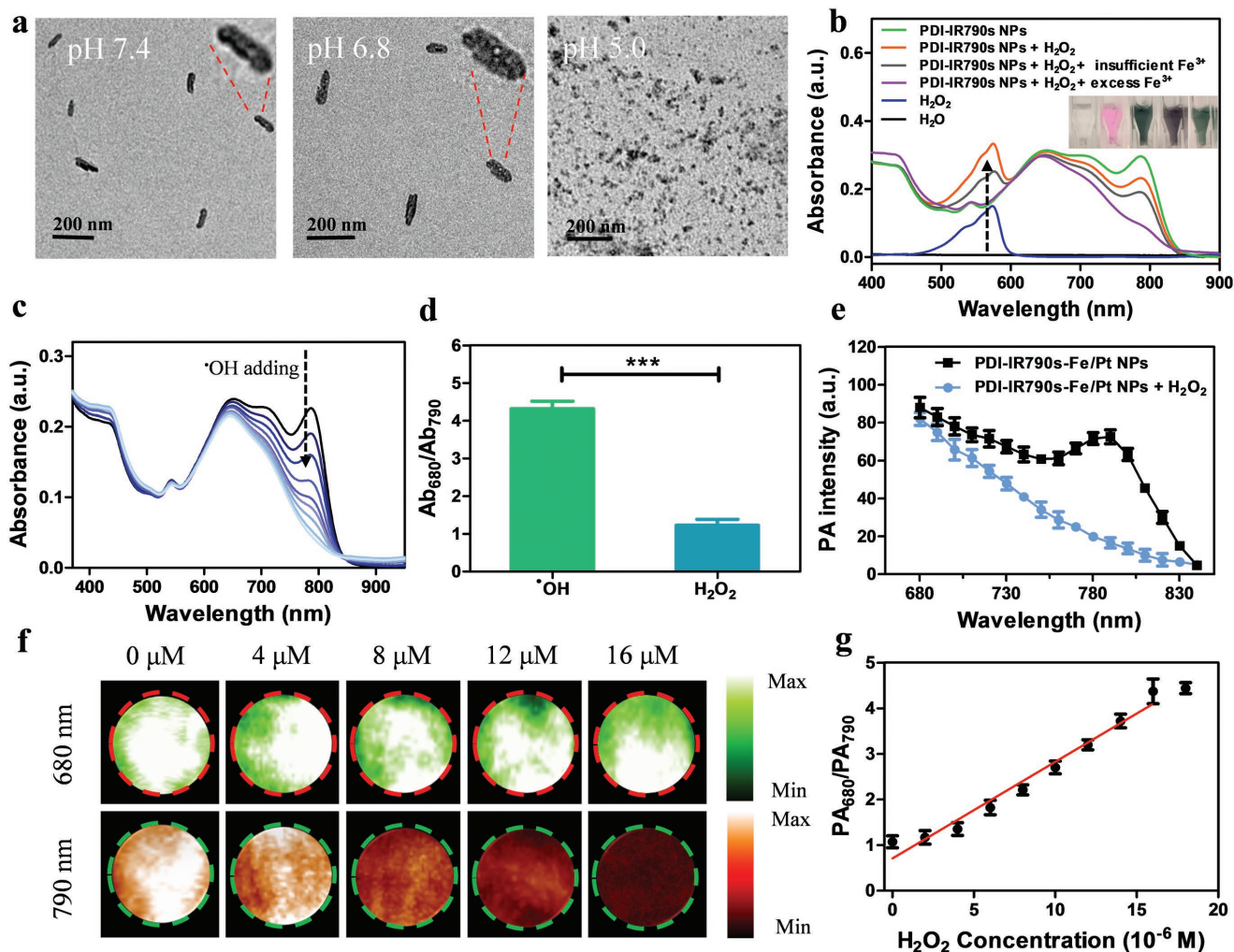


Figure 2. Characterization and in vitro ratiometric PA imaging of ROS from the theranostic PDI-IR790s-Fe/Pt NPs. a) Representative TEM images of the PDI-IR790s-Fe/Pt NPs treated with different pH buffers for 24 h. b) UV-vis spectra of different solutions treated with Amplex Red H_2O_2 activity kit, indicating the consumption of H_2O_2 in the presence Fe^{3+} catalyst. (Inset photographs (from right to left): water, H_2O_2 , PDI-IR790s NPs, PDI-IR790s NPs plus H_2O_2 , PDI-IR790s NPs plus H_2O_2 and excess Fe^{3+} , all with H_2O_2 activity kit). c) UV-vis absorption spectra of PDI-IR790s NP solutions after adding $\cdot\text{OH}$. d) The reactivity of PDI-IR790s NPs to H_2O_2 and $\cdot\text{OH}$ in PBS (pH = 7.4). (*P* values, $***P < 0.001$, are calculated by *t* test.) e) Representative PA spectra of the PDI-IR790s-Fe/Pt NPs with or without H_2O_2 treatment. f) PA images of the PDI-IR790s-Fe/Pt NP solution at 680 and 790 nm treated with increased concentrations of H_2O_2 (from right to left). g) The $\text{PA}_{680}/\text{PA}_{790}$ ratio of the PDI-IR790s-Fe/Pt NPs as a function of the concentration of H_2O_2 in PBS (pH = 7.4).

($\text{PA}_{680}/\text{PA}_{790}$) showed linear correlation with H_2O_2 concentration (Figure 2g). The $\text{PA}_{680}/\text{PA}_{790}$ ratio at a saturation point (4.37 ± 0.27) was around fourfold higher than that at the initial inactive state (1.07 ± 0.13). Such high accuracy and sensitivity of PDI-IR790s-Fe/Pt NPs in the ratiometric PA imaging of $\cdot\text{OH}$ may provide the possibility to visualize ROS generation in living mice.

Additionally, we conducted an experiment to monitor intracellular generation and self-monitoring of ROS from PDI-IR790s-Fe/Pt NPs. A compound, 2',7'-dichlorodihydrofluorescein diacetate (H2DCFDA), was employed as an ROS indicator. It can be activated by ROS and converted to green-fluorescent 2',7'-dichlorofluorescein. Compared with the control/untreated cells, in which green fluorescence signal was not detected, cells treated with PDI-IR790s-Fe/Pt NPs for 6 h exhibited green fluorescence signal in the cytoplasm

(Figure 3a). The fluorescence signal was further amplified when the incubation time was increased to 12 h, indicating that ROS generated inside the cells was further increased (Figure 3a). The results demonstrated in vitro generation of $\cdot\text{OH}$ from the increasing H_2O_2 was enhanced by PDI-IR790s-Fe/Pt NPs. In contrast, fluorescence signal was not observed in cells treated with PDI-IR790s NPs in the absence of Fe^{3+} ; it is evident that no ROS were generated without the Fenton reaction (Figure S19, Supporting Information).

The cytotoxic effect of PDI-IR790s-Fe/Pt NPs on U87MG cells was further evaluated using 3-(4,5-dimethylthiazol-2-yl)-2,5-diphenyltetrazolium bromide (MTT) assay (Figure 3b). PDI-IR790s NP exhibited nearly no toxicity to U87MG cells (Figure S20, Supporting Information). Small molecular cisplatin prodrug and free cisplatin and (carboxylic cisplatin) containing the same platinum content were used as controls. While

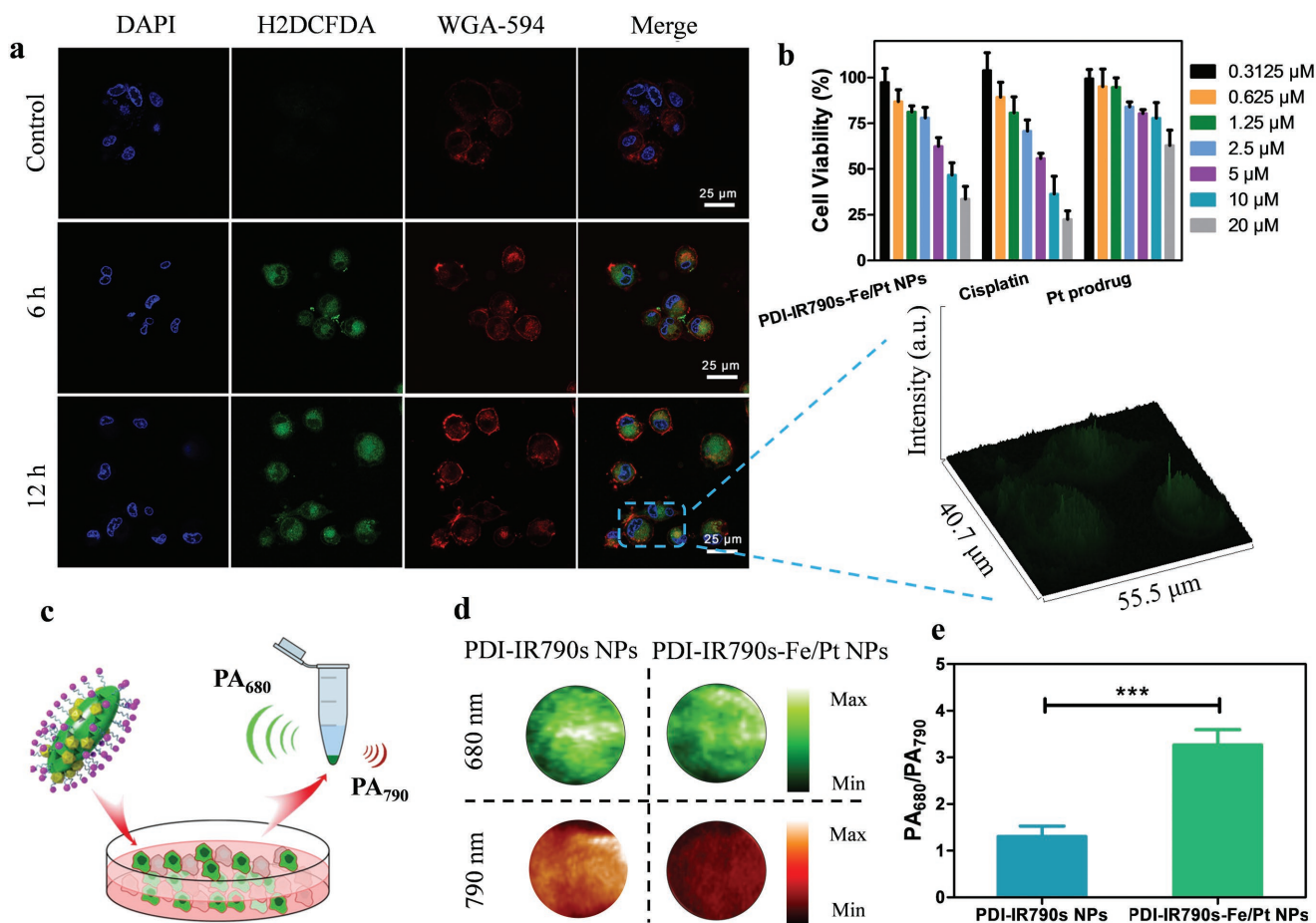


Figure 3. In vitro ROS generation and cytotoxicity of theranostic PDI-IR790s-Fe/Pt NPs. a) Confocal microscopy images of U87MG cells incubated without (control cells) and with PDI-IR790s-Fe/Pt NPs for 6 and 12 h. (Blue color: nuclei stained by DAPI, red color: cell membrane stained by WGA-594, green color: ROS indicator of H2DCFDA). The increasing intensity of the green signal of H2DCFDA in the cell represented the enhanced ROS generation from PDI-IR790s-Fe/Pt NPs. b) The cytotoxicity of the different formulations after 48 h incubation. c) Schematic illustration of the cancer cells treated with PDI-IR790s-Fe/Pt NPs followed by concentration for ratiometric PA imaging. PA images d) and ratiometric PA signals ($\text{PA}_{680}/\text{PA}_{790}$) e) of the concentrated cancer cells treated with PDI-IR790s NPs or PDI-IR790s-Fe/Pt NPs. (P values, $***P < 0.001$, are calculated by t test.)

PDI-IR790s-Fe/Pt NPs and free cisplatin exhibited similar cytotoxic effect against U87MG cells (half maximal inhibitory concentration (IC_{50}) values were 9.01 and 5.98×10^{-6} M, respectively), cisplatin prodrug exhibited very weak cytotoxicity. These observations showed that combining ferric ions with anticancer drug cisplatin may induce H_2O_2 production, thus enhancing hydroxyl radical formation, leading to apoptosis, and eventually, sensitizing the anticancer drug (Figure 1b). This demonstration shows a new strategy in which ferric ions were used to deliver H_2O_2 -inducing cancer therapy based on combined actions.

In vitro ratiometric PA imaging was further performed to monitor ROS generation as a result of theranostic NP uptake in cancer cells (Figure 3c). After the cells were treated with PDI-IR790s NPs or PDI-IR790s-Fe/Pt NPs for 8 h, the PA signals were simultaneously monitored at 680 and 790 nm, as illustrated by pseudo green and red colors, respectively (Figure 3d). In comparison to strong PA signal at 790 nm in cells treated with PDI-IR790s NPs, cells treated with PDI-IR790s-Fe/Pt NPs exhibited weak signal, indicating that ROS were generated through Fenton reaction, and further reacted with IR790s. Moreover, the $\text{PA}_{680}/\text{PA}_{790}$ ratio of the

PDI-IR790s-Fe/Pt NP-treated cells (3.25 ± 0.35) was significantly higher than that of PDI-IR790s-treated cells (1.31 ± 0.25) (Figure 3e). The results demonstrated that the PDI-IR790s-Fe/Pt NPs not only could generate ROS and induce toxicity but could also measure the ROS generation through ratiometric PA imaging.

To demonstrate the capability of the ratiometric PA imaging in the detection of ROS generation in vivo, PDI-IR790s-Fe/Pt NPs or PDI-IR790s NPs ($10 \mu\text{L}$, 1 mg mL^{-1}) were administered locally and subcutaneously to U87MG xenograft tumors. PA images at 680 and 790 nm were captured at 0.5 and 6 h postinjection (Figure 4a,b). PA intensities at 680 nm captured at 0.5 and 6 h postinjection were similar in both samples, indicating that PDIs were stable inside the tumors. However, PA intensity at 790 nm of the tumors treated with PDI-IR790s-Fe/Pt NPs at 6 h postinjection decreased by a certain extent, indicating that the reaction between the generated ROS and IR790s took place. Such specific ratiometric response could easily be distinguished in the PA images. On the other hand, PA signals at 790 nm of the tumors treated with PDI-IR790s NPs at 0.5 and 6 h postincubation were not significantly different, indicating that ROS

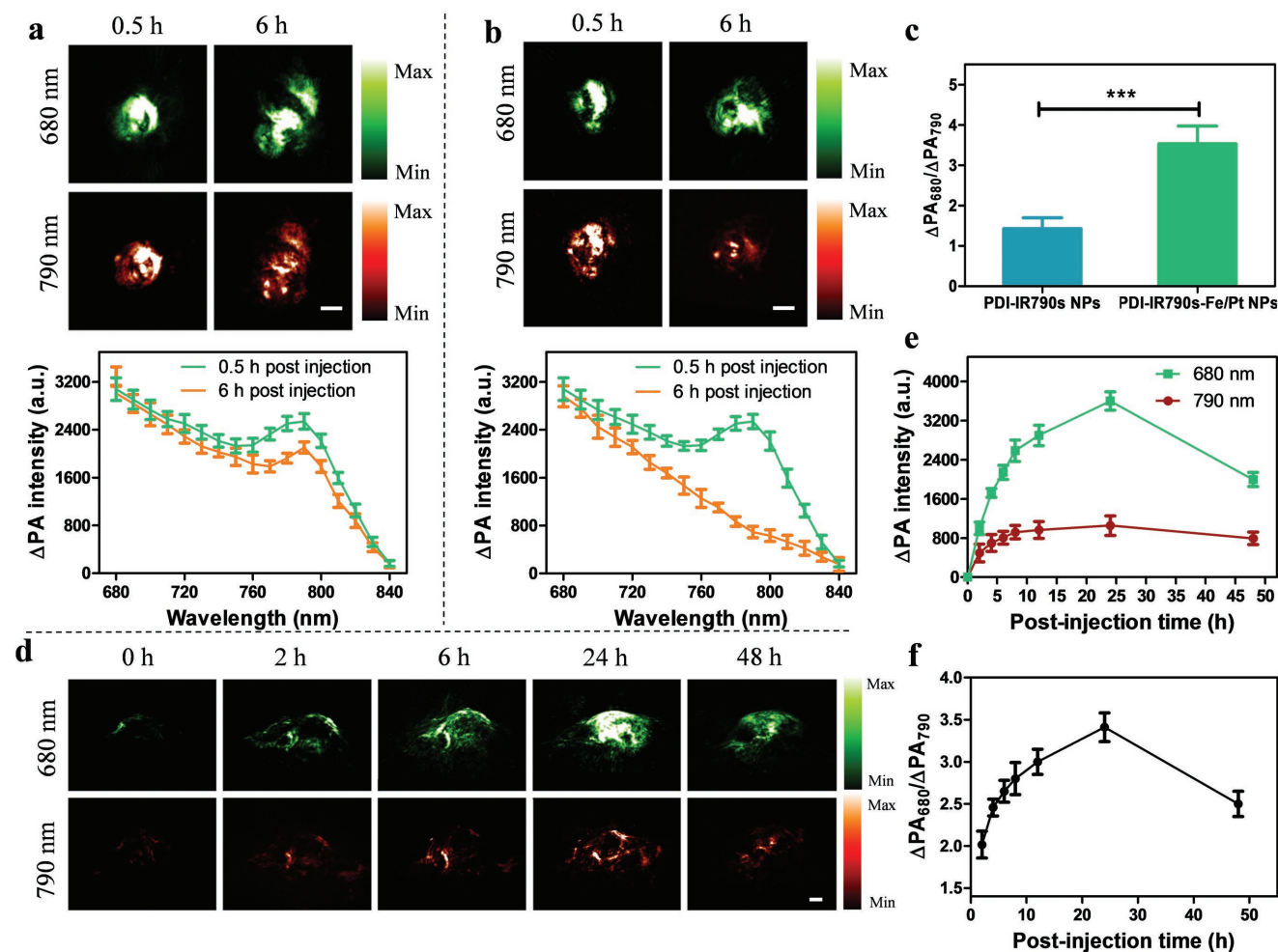


Figure 4. In vivo ratiometric PA imaging of ROS generation. PA images and spectra of the tumor with local administration of PDI-IR790s NPs a) and PDI-IR790s-Fe/Pt NPs b) recorded at postinjection time of 0.5 and 6 h, respectively (Scale bar, 2 mm). c) Ratiometric PA signals ($\Delta PA_{680}/\Delta PA_{790}$) after local injection of PDI-IR790s NPs and PDI-IR790s-Fe/Pt NPs at 6 h postinjection. (*P* values, $***P < 0.001$, are calculated by *t* test.) d) Representative PA images at 680 and 790 nm of a subcutaneous U87MG tumor after intravenous injection of PDI-IR790s-Fe/Pt NPs at different postinjection times. e) PA intensity increment at 680 nm (ΔPA_{680}) and 790 nm (ΔPA_{790}) as a function of postinjection time of the PDI-IR790s-Fe/Pt NPs in tumor-bearing mice (*n* = 3) (Scale bar, 2 mm). f) The ratiometric PA signals ($\Delta PA_{680}/\Delta PA_{790}$) in the tumor as a function of postinjection time of PDI-IR790s-Fe/Pt NPs (*n* = 3).

generation in the tumors was not enhanced. The PA images and the spectral data confirmed that interaction between ROS and IR790s occurred in the tumors of mice treated with PDI-IR790s-Fe/Pt NPs, but not in mice treated with PDI-IR790s NPs. To minimize the tissue interference during PA testing, ΔPA , a veritable PA intensity of NPs in the tumor was defined. The value was obtained by deducting the endogenous tissue intensity (e.g., absorption of oxy- and deoxyhemoglobins), which was used to evaluate the ratiometric PA signals ($\Delta PA_{680}/\Delta PA_{790}$) in vivo. The ratiometric $\Delta PA_{680}/\Delta PA_{790}$ of the tumors treated with PDI-IR790s-Fe/Pt NPs (3.53 ± 0.44) was 2.5-fold higher than that of PDI-IR790s NPs (1.43 ± 0.32) (Figure 4c). Thus, the significantly enhanced ratiometric PA signal of PDI-IR790s-Fe/Pt NPs in tumors indicated its ability to monitor ROS generation during use in chemotherapy.

To visualize ROS generation during cancer chemotherapy by ratiometric PA imaging in vivo, U87MG tumor-bearing mice were intravenously injected (i.v.) with PDI-IR790s-

Fe/Pt NPs. The injected dosage was 200 μL of theranostic NPs in PBS (5 mg mL^{-1} , based on PDI prodrug content). The PA images at 680 and 790 nm were recorded by pseudo green and red colors, respectively (Figure 4d). The PA signal increment at 680 nm (ΔPA_{680}) in PDI-IR790s-Fe/Pt NP-treated mice was substantially increased, and this may be attributed to enhanced permeability and retention effect of the theranostic NPs (Figure 4e). In contrast, the increase of ΔPA_{790} was lower than that of ΔPA_{680} (Figure 4e), indicating the reaction between generated ROS and IR790s occurred in the tumors. Owing to such great signal differences, the in vivo ratiometric PA signal ($\Delta PA_{680}/\Delta PA_{790}$) for the treated mice gradually increased and reached its maximum at ≈ 24 h postinjection (Figure 4f). At 24 h postinjection, the $\Delta PA_{680}/\Delta PA_{790}$ reached a plateau at 3.41 ± 0.13 , which was ≈ 1.7 -fold higher than that of the 2 h postinjection (2.01 ± 0.16). *N*-acetyl-L-cysteine (NAC) is an antioxidant drug with the ability to scavenge ROS and reduce ROS level in the tumor. As a negative control experiment, ratiometric

PA imaging of PDI-IR790s-Fe/Pt NPs on NAC-treated mice was used to verify the stability of the loaded IR790s in the NPs during blood circulation and in the tumor with low ROS level (Figure S21, Supporting Information).^[30] After injection of the PDI-IR790s-Fe/Pt NPs to the NAC-pretreated mice, the $\Delta PA_{680}/\Delta PA_{790}$ value was only 1.55 ± 0.15 at 24 h postinjection, indicating low ROS level in the NAC-pretreated tumors. These data not only validated the enhanced ROS generation due to the theranostic PDI-IR790s-Fe/Pt NPs in tumors but also highlighted the ability of in vivo ratiometric PA imaging to visualize and monitor ROS levels in real time, after the NP treatment.

These promising results motivated us to further evaluate the antitumor performance of the PDI-IR790s-Fe/Pt NPs in vivo. Mice bearing U87MG tumors were randomly divided into five groups, each of which were administered with different compounds, including PBS, PDI-IR790s NPs, free prodrug, cisplatin, and PDI-IR790s-Fe/Pt NPs. The tumors of mice treated with PDI-IR790s NPs and prodrug were found to grow very quickly (Figure 5a), indicating that the compounds had poor antitumor efficacy. As expected, PDI-IR790s-Fe/Pt NPs effectively inhibited tumor growth due to the synergistic therapeutic effect of cisplatin drugs and enhanced ROS ($\cdot\text{OH}$) generation (based on Fenton reaction). Compared with other compounds, the survival rate of the PDI-IR790s-Fe/Pt NP-treated mice was higher (Figure 5b). There was no significant body weight loss observed during the therapeutic process (Figure S22, Supporting Information), suggesting that the theranostic NP platform has high

biocompatibility and biosafety. In addition, apoptosis and necrosis of tumor cells were observed by the hematoxylin and eosin (H&E)-stained tumor sections collected at day 18 in the PDI-IR790s-Fe/Pt NP-treated group, which is consistent with the anticancer therapy effect of the theranostic NPs (Figure 5c,d). The results suggested that cisplatin and ferric ions delivered through PDI-IR790s-Fe/Pt NPs could enhance ROS generation while providing synergistic tumor therapeutic efficacy.

In conclusion, we developed a strategy for the delivery of ROS-inducing anticancer drug cisplatin and ferric ions through a semiconducting organic nanoplatform. The nanoplatform preferentially increases ROS generation at the tumor site, while levels of ROS generation are monitored through ratiometric PA imaging. The cisplatin prodrug-encapsulated theranostic platform can rapidly disintegrate into cisplatin that subsequently forms Pt-DNA adducts, leading to activation of NOXs. Such activation then triggers a reaction cascade, resulting in increased formation of H_2O_2 . The loaded ferric ions can catalyze H_2O_2 decomposition into highly toxic ROS within cancer cells, leading to rapid oxidation and deterioration of cellular membranes. A ROS indicator, IR790s, which was integrated into the PDI nanoplatform, exhibited high detection sensitivity to ROS through ratiometric PA imaging, both in vitro and in vivo. The combination of cisplatin and enhanced ROS generation exhibited strong combination antitumor efficacy in vivo. Summarily, the multifunctional PDI-IR790s-Fe/Pt NPs with facile preparation, real-time

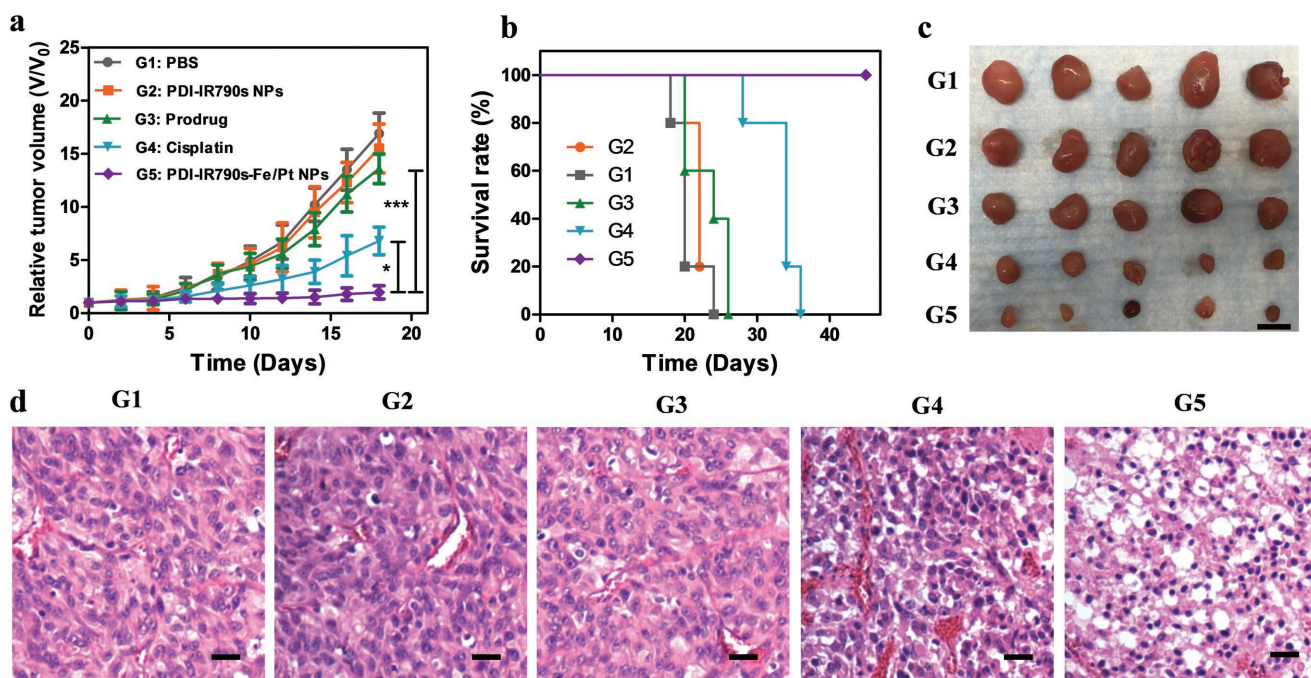


Figure 5. In vivo combined cancer therapy of PDI-IR790s-Fe/Pt NPs. a) Xenograft tumor volume growth curves in different treatment groups: G1–G5, namely PBS, PDI-IR790s NPs, free prodrug, cisplatin, PDI-IR790s-Fe/Pt (different groups with the same Pt dose). The above results indicate the PDI-IR790s-Fe/Pt NPs have strong therapeutic effect on U87MG tumor. (*P* values, $*P < 0.05$, $***P < 0.001$, are calculated by *t* test.) b) The survival rate curves of xenograft tumor bearing mice with various treatments of G1–G5. (c) Resected U87MG tumors in different treatment groups on day 18 (Scale bar, 10 mm). d) The H&E stained images of tumor sections after various treatments of G1–G5 (Scale bar, 20 μm). Compared with the control groups, the tumor cells in the PDI-IR790s-Fe/Pt NPs treated group developed larger necrotic areas, which show strong tumor inhibition efficacy of the theranostic NPs.

monitoring ability, and synergistic efficacy may potentially be used to provide real-time ratiometric PA imaging in situ for guided cancer therapy.

Supporting Information

Supporting Information is available from the Wiley Online Library or from the author.

Acknowledgements

Z.Y. and Y.D. contributed equally to this work. This work was supported by the Intramural Research Program of the National Institute of Biomedical Imaging and Bioengineering (NIBIB), the National Institutes of Health (NIH), the National Natural Science Foundation of China (Nos. 21674048, 21574064, and 61378081), and the Natural Science Foundation of Jiangsu Province of China (Nos. NY211003 and BM2012010).

Conflict of Interest

The authors declare no conflict of interest.

Keywords

cisplatin, ratiometric photoacoustic imaging, ROS generation, synergistic cancer therapy, theranostics

Received: December 23, 2017

Revised: February 6, 2018

Published online: April 30, 2018

- [1] Z. Zhou, J. Song, L. Nie, X. Chen, *Chem. Soc. Rev.* **2016**, *45*, 6597.
- [2] W. Fan, P. Huang, X. Chen, *Chem. Soc. Rev.* **2016**, *45*, 6488.
- [3] Q. Miao, C. Xie, X. Zhen, Y. Lyu, H. Duan, X. Liu, J. V. Jokerst, K. Pu, *Nat. Biotechnol.* **2017**, *35*, 1102.
- [4] X. Zhen, C. Zhang, C. Xie, Q. Miao, K. L. Lim, K. Pu, *ACS Nano* **2016**, *10*, 6400.
- [5] G.-Y. Liou, P. Storz, *Free Radical Res.* **2010**, *44*, 479.
- [6] S. E. Weinberg, N. S. Chandel, *Nat. Chem. Biol.* **2015**, *11*, 9.
- [7] B. Halliwell, M. V. Clement, L. H. Long, *FEBS Lett.* **2000**, *486*, 10.
- [8] C. C. Winterbourn, *Toxicol. Lett.* **1995**, *82*, 969.
- [9] J. Kim, H. R. Cho, H. Jeon, D. Kim, C. Song, N. Lee, S. H. Choi, T. Hyeon, *J. Am. Chem. Soc.* **2017**, *139*, 10992.
- [10] Z. Zhou, J. Song, R. Tian, Z. Yang, G. Yu, L. Lin, G. Zhang, W. Fan, F. Zhang, G. Niu, L. Nie, X. Chen, *Angew. Chem., Int. Ed.* **2017**, *129*, 6592.
- [11] C. Zhang, W. Bu, D. Ni, S. Zhang, Q. Li, Z. Yao, J. Zhang, H. Yao, Z. Wang, J. Shi, *Angew. Chem., Int. Ed.* **2016**, *128*, 2141.
- [12] Y. Dai, H. Xiao, J. Liu, Q. Yuan, P. a. Ma, D. Yang, C. Li, Z. Cheng, Z. Hou, P. Yang, J. Lin, *J. Am. Chem. Soc.* **2013**, *135*, 18920.
- [13] P. a. Ma, H. Xiao, C. Li, Y. Dai, Z. Cheng, Z. Hou, J. Lin, *Mater. Today* **2015**, *18*, 554.
- [14] Y. Dai, C. Xu, X. Sun, X. Chen, *Chem. Soc. Rev.* **2017**, *46*, 3830.
- [15] Y. Dai, J. Guo, T. Y. Wang, Y. Ju, A. J. Mitchell, T. Bonnard, J. Cui, J. J. Richardson, C. E. Hagemeyer, K. Alt, F. Caruso, *Adv. Healthcare Mater.* **2017**, *6*, 1700467.
- [16] T. Itoh, R. Terazawa, K. Kojima, K. Nakane, T. Deguchi, M. Ando, Y. Tsukamasa, M. Ito, Y. Nozawa, *Free Radical Res.* **2011**, *45*, 1033.
- [17] H.-J. Kim, J.-H. Lee, S.-J. Kim, G. S. Oh, H.-D. Moon, K.-B. Kwon, C. Park, B. H. Park, H.-K. Lee, S.-Y. Chung, *J. Neurosci.* **2010**, *30*, 3933.
- [18] P. a. Ma, H. Xiao, C. Yu, J. Liu, Z. Cheng, H. Song, X. Zhang, C. Li, J. Wang, Z. Gu, *Nano Lett.* **2017**, *17*, 928.
- [19] J. F. Lovell, C. S. Jin, E. Huynh, H. Jin, C. Kim, J. L. Rubinstein, W. C. Chan, W. Cao, L. V. Wang, G. Zheng, *Nat. Mater.* **2011**, *10*, 324.
- [20] Y. Lyu, K. Pu, *Adv. Sci.* **2017**, *4*, 1600481.
- [21] C. Xie, X. Zhen, Q. Lei, R. Ni, K. Pu, *Adv. Funct. Mater.* **2017**, *27*, 1605397.
- [22] J. Song, X. Yang, O. Jacobson, P. Huang, X. Sun, L. Lin, X. Yan, G. Niu, Q. Ma, X. Chen, *Adv. Mater.* **2015**, *27*, 4910.
- [23] X. Wang, Y. Pang, G. Ku, X. Xie, G. Stoica, L. V. Wang, *Nat. Biotechnol.* **2003**, *21*, 803.
- [24] M. Xu, L. V. Wang, *Rev. Sci. Instrum.* **2006**, *77*, 041101.
- [25] K. Cheng, S.-R. Kothapalli, H. Liu, A. L. Koh, J. V. Jokerst, H. Jiang, M. Yang, J. Li, J. Levi, J. C. Wu, S. S. Gambhir, Z. Cheng, *J. Am. Chem. Soc.* **2014**, *136*, 3560.
- [26] Y. Lyu, D. Cui, H. Sun, Y. Miao, H. Duan, K. Pu, *Angew. Chem., Int. Ed.* **2017**, *56*, 9155.
- [27] C. Xie, X. Zhen, Y. Lyu, K. Pu, *Adv. Mater.* **2017**, *29*, 1703693.
- [28] Q. Miao, K. Pu, *Bioconjugate Chem.* **2016**, *27*, 2808.
- [29] Y. Lyu, X. Zhen, Y. Miao, K. Pu, *ACS Nano* **2017**, *11*, 358.
- [30] J. Zhang, X. Zhen, P. K. Upputuri, M. Pramanik, P. Chen, K. Pu, *Adv. Mater.* **2017**, *29*, 1604764.
- [31] K. Yang, L. Zhu, L. Nie, X. Sun, L. Cheng, C. Wu, G. Niu, X. Chen, Z. Liu, *Theranostics* **2014**, *4*, 134.
- [32] H. Li, P. Zhang, L. P. Smaga, R. A. Hoffman, J. Chan, *J. Am. Chem. Soc.* **2015**, *137*, 15628.
- [33] Q. Chen, X. Liu, J. Chen, J. Zeng, Z. Cheng, Z. Liu, *Adv. Mater.* **2015**, *27*, 6820.
- [34] Q. Miao, Y. Lyu, D. Ding, K. Pu, *Adv. Mater.* **2016**, *28*, 3662.
- [35] Y. Liu, S. Wang, Y. Ma, J. Lin, H. Y. Wang, Y. Gu, X. Chen, P. Huang, *Adv. Mater.* **2017**, *29*, 1606129.
- [36] C. Yin, X. Zhen, Q. Fan, W. Huang, K. Pu, *ACS Nano* **2017**, *11*, 4174.
- [37] D. Oushiki, H. Kojima, T. Terai, M. Arita, K. Hanaoka, Y. Urano, T. Nagano, *J. Am. Chem. Soc.* **2010**, *132*, 2795.
- [38] Q. Chen, C. Liang, X. Sun, J. Chen, Z. Yang, H. Zhao, L. Feng, Z. Liu, *Proc. Natl. Acad. Sci. USA* **2017**, *114*, 5343.
- [39] A. J. Shuhendler, K. Pu, L. Cui, J. P. Uetrecht, J. Rao, *Nat. Biotechnol.* **2014**, *32*, 373.
- [40] J. Peng, A. Samanta, X. Zeng, S. Han, L. Wang, D. Su, D. T. B. Loong, N. Y. Kang, S. J. Park, A. H. All, W. Jiang, L. Yuan, X. Liu, Y. T. Chang, *Angew. Chem., Int. Ed.* **2017**, *56*, 4165.
- [41] K. Pu, A. J. Shuhendler, J. V. Jokerst, J. Mei, S. S. Gambhir, Z. Bao, J. Rao, *Nat. Nanotechnol.* **2014**, *9*, 233.
- [42] R. Dobrawa, M. Lysetska, P. Ballester, M. Grüne, F. Würthner, *Macromolecules* **2005**, *38*, 1315.
- [43] Z. Yang, R. Tian, J. Wu, Q. Fan, B. C. Yung, G. Niu, O. Jacobson, Z. Wang, G. Liu, G. Yu, W. Huang, X. Chen, *ACS Nano* **2017**, *11*, 4247.
- [44] C. Cui, Z. Yang, X. Hu, J. Wu, K. Shou, H. Ma, C. Jian, Y. Zhao, B. Qi, X. Hu, Ai. Yu, Q. Fan, *ACS Nano* **2017**, *11*, 3298.
- [45] Q. Fan, K. Cheng, Z. Yang, R. Zhang, M. Yang, X. Hu, X. Ma, L. Bu, X. Lu, X. Xiong, W. Huang, H. Zhao, Z. Cheng, *Adv. Mater.* **2015**, *27*, 843.
- [46] Z. Yang, J. Song, Y. Dai, J. Chen, F. Wang, L. Lin, Y. Liu, F. Zhang, G. Yu, Z. Zhou, W. Fan, W. Huang, Q. Fan, X. Chen, *Theranostics* **2017**, *7*, 2177.
- [47] W. Cheng, H. Cheng, S. Wan, X. Zhang, M. Yin, *Chem. Mater.* **2017**, *29*, 4218.